

Another Look at Interannual-to-Interdecadal Variations of the East Asian Winter Monsoon: The Northern and Southern Temperature Modes

BIN WANG

Department of Meteorology, and IPRC, University of Hawaii at Manoa, Honolulu, Hawaii

ZHIWEI WU

LASG, Institute of Atmospheric Physics, Chinese Academy of Sciences, Beijing, China, and Department of Meteorology, and IPRC, University of Hawaii at Manoa, Honolulu, Hawaii

CHIH-PEI CHANG

Department of Meteorology, Naval Postgraduate School, Monterey, California, and Department of Atmospheric Sciences, National Taiwan University, Taipei, Taiwan

JIAN LIU

State Key Laboratory of Lake Science and Environment, Nanjing Institute of Geography and Limnology, Chinese Academy of Sciences, Nanjing, China

JIANPING LI AND TIANJUN ZHOU

LASG, Institute of Atmospheric Physics, Chinese Academy of Sciences, Beijing, China

(Manuscript received 14 May 2009, in final form 12 October 2009)

ABSTRACT

This study investigates the causes of interannual-to-interdecadal variability of the East Asian (EA; 0°–60°N, 100°–140°E) winter monsoon (EAWM) over the past 50 yr (1957–2006). The winter mean surface air temperature variations are dominated by two distinct principal modes that together account for 74% of the total temperature variance. The two modes have notably different circulation structures and sources of variability. The northern mode, characterized by a westward shift of the EA major trough and enhanced surface pressure over central Siberia, represents a cold winter in the northern EA resulting from cold-air intrusion from central Siberia. The southern mode, on the other hand, features a deepening EA trough and increased surface pressure over Mongolia, representing a cold winter south of 40°N resulting from cold-air intrusion from western Mongolia. The cold northern mode is preceded by excessive autumn snow covers over southern Siberia–Mongolia, whereas the cold southern mode is preceded by development of La Niña episodes and reduced snow covers over northeast Siberia. These remarkably different spatiotemporal structures and origins are primarily associated with interannual variations. On the decadal or longer time scale their structures are somewhat similar and are preceded by similar autumn sea surface temperature anomalies over the North Atlantic and tropical Indian Ocean. The two modes found for the EA region also represent the winter temperature variability over the entire Asian continent. Thus, study of the predictability of the two modes may shed light on understanding the predictable dynamics of the Asian winter monsoon.

Corresponding author address: Bin Wang, Post 401, 1680 East-West Rd., Honolulu, HI 96822.
E-mail: wangbin@hawaii.edu

1. Introduction

The East Asian (EA) winter monsoon (EAWM) is associated with a most powerful circulation system—the Siberian–Mongolian High (SMH)—in the earth’s atmosphere resulting from the large thermal contrast between the world’s largest landmass, Eurasia, and the Indo-Pacific Ocean (e.g., Li 1955; Tao 1957; Ding 1994). The variability of the EAWM dominates Asian–Pacific winter climate fluctuations and influences tropical variability as well as the North American climate through changing positions of tropical heat sources and their associated teleconnections (e.g., Chang and Lau 1982; Lau and Chang 1987; Yasunari 1991; Wang and Li 2004). The EAWM exhibits large-amplitude year-to-year fluctuations, which have been a subject of extensive investigation in the last decade or so. The EAWM variation has been recognized to respond to El Niño–Southern Oscillation (ENSO; e.g., Zhang et al. 1996; Tomita and Yasunari 1996; Ji et al. 1997; Wang et al. 2000; Hamada et al. 2002; Chang et al. 2004; Chan and Li 2004). Several recent studies described how the EAWM variation is related to the Arctic Oscillation (AO), the North Atlantic Oscillation (NAO), and the Southern Hemisphere annular mode on the decadal time scale, or to the global warming trend in the recent decades (e.g., Gong et al. 2001; Jhun and Lee 2004; Wu et al. 2006; Li and Bates 2007; Wu et al. 2009). Comprehensive reviews of the EAWM are presented by Chang et al. (2006), Ding and Sikka (2006), and Chang et al. (2010).

The EAWM system may be viewed as a coupled extratropical–tropical system. As shown in Fig. 1a, a salient high pressure ridge extends from the SMH all the way down to the northern South China Sea, reflecting the recurrent tracks of cold air mass outbreaks from its source region—the Siberian cold dome (Ding and Krishnamurti 1987; Ding 1990; Zhang et al. 1997; Compo et al. 1999). The corresponding boundary layer *northerlies* prevail from 60°N down to the equator. The interaction of monsoon cold surges with the terrain and with tropical intraseasonal oscillation can induce great variability in convection and rainfall in the southern South China Sea, the Philippines, the Indo-China Peninsula, and the northern Maritime Continent (Chang and Lau 1980; Chang et al. 1983, 2004, 2006, 2010; Matsumoto 1992; Fig. 1b). The latent heat released by the intense, near-equatorial convective precipitation in turn affects the upper branch of local meridional circulation, accelerating the upper-troposphere EA westerly jet (Chang and Lau 1980, 1982; Lau and Chang 1987; Murakami 1987; Yang et al. 2002; Fig. 1b), and enhances the baroclinic development along and downstream of the jet, affecting both the EA major trough and the winter storm track

from the western North Pacific to North America (Chang et al. 2006). Thus, the SMH, the mid- to upper-level EA major trough, the upper-tropospheric EA jet, and the near-equatorial convection are dynamically coupled and may be viewed as an integrated EAWM circulation system.

One of the unique features of the EAWM is its extremely large meridional extent stretching from the polar region to the equator. The previous studies, however, tend to measure the strength of EAWM using a single index (e.g., Guo 1983; Ji et al. 1997; Lu and Chan 1999; Cui and Sun 1999; Chen et al. 2000; Li and Zeng 2002; Jhun and Lee 2004; Wu et al. 2006). Given this large meridional extent, the EAWM variability may differ between the extratropical and tropical EA, because the circulation systems in the two regions are different and the degree of their coupling with near-equatorial convection are also different. This motivated the present reexamination of the EAWM variability by focusing on meridional differences in the anomaly patterns and their origins, as shown in Section 3.

Most previous studies of the EAWM variability have also taken circulation variables as measures of its strength (e.g., Guo 1983; Ji et al. 1997; Lu and Chan 1999; Cui and Sun 1999; Chen et al. 2000; Li and Zeng 2002; Jhun and Lee 2004; Wu et al. 2006). Different from these studies, we choose surface air temperature as the key variable because the degree of coldness is often an important indicator on the severity of the winter weather, and the temperature variation has better spatial homogeneity than that of precipitation and surface winds over complex terrain. Study of temperature variability may provide an alternative perspective for the EAWM climate variability.

The purpose of this study is to investigate the principal modes of interannual (IA)-to-interdecadal (ID) variability of the EAWM and the origins of these principal modes. We found that the surface air temperature of the EAWM is dominated by two distinct modes of variability: one with the largest amplitude in the northern domain and the other in the southern domain (section 3). The two modes have notably different three-dimensional circulation structures (section 4), which mainly originate from the IA variation (section 5). The two modes also have different sources of predictability on the IA time scale (section 6). On the ID time scale, they share some common characteristics and have similar sources of predictability (sections 5 and 6). Section 7 discusses the physical processes by which the lower boundary anomalous forcing generates the EAWM variability. The last section summarizes major findings and discusses future work.

2. Data

Winter (December–February) seasonal mean data were used for analysis of the IA-to-ID variations. The

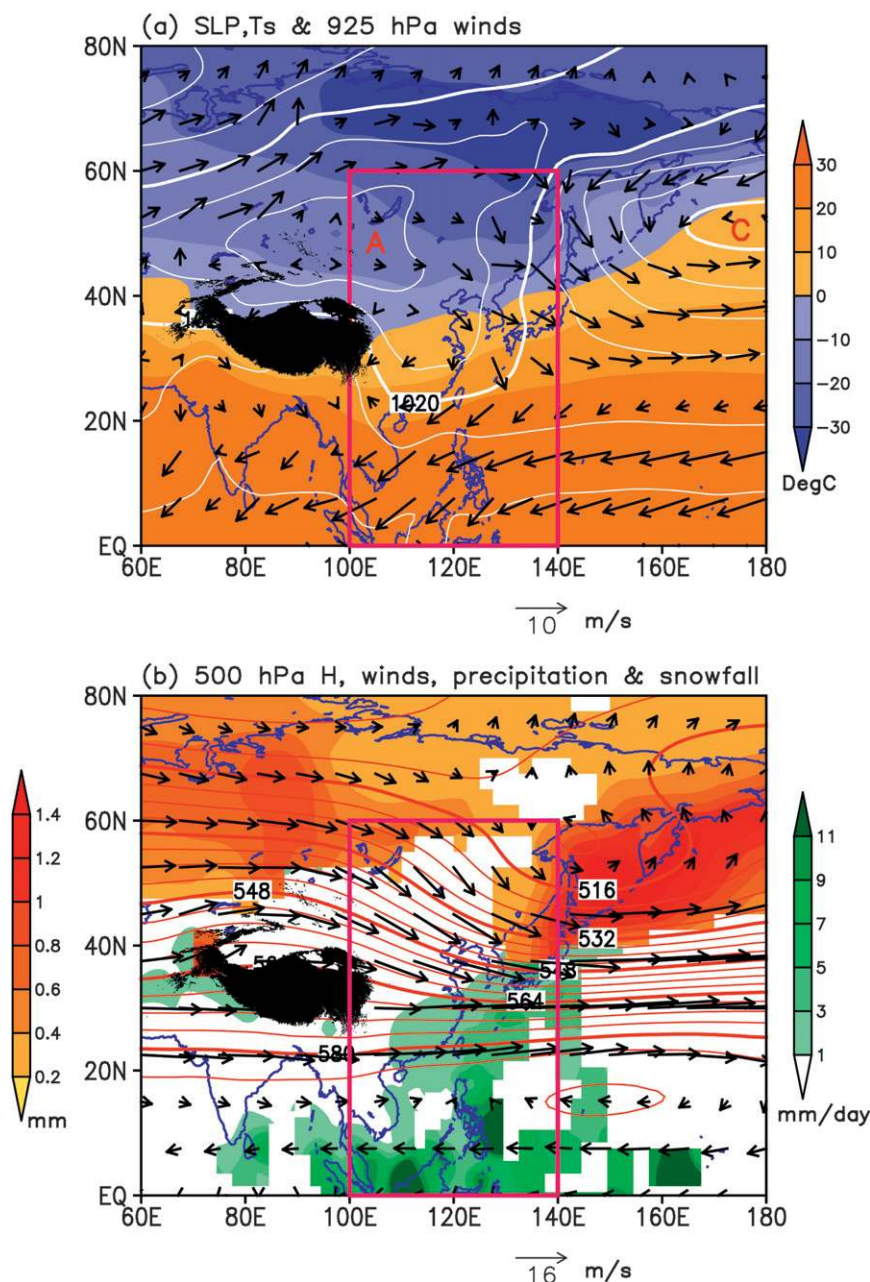


FIG. 1. Climatological winter (December–February) mean (a) SLP (contours with intervals of 5 hPa), Ts (color shadings, °C), and 925-hPa winds (vectors, m s⁻¹), and (b) 500-hPa geopotential height (contours with interval of 40 gpm), winds (vectors, m s⁻¹), precipitation (green shadings, mm day⁻¹), and snowfall (yellow–red shadings, mm water equivalent) derived from ERA-40 datasets (Uppala et al. 2005). “A” and “C” denote anticyclonic and cyclonic circulations, respectively. The boxed area indicates the East Asian winter monsoon domain.

primary data used in this study cover the period from December 1957 to February 2007. Because over East Asia the National Centers for Environmental Prediction–National Center for Atmospheric Research (NCEP–NCAR) Global Reanalysis 1 (NCEP-1; Kalnay et al. 1996) data may have systematic errors in the period

before 1980 (Wu et al. 2005), we decided to use the 40-yr European Centre for Medium-Range Weather Forecasts (ECMWF) Re-Analysis (ERA-40; Uppala et al. 2005) for the period of 1957–2001, and we extend the data from December 2002 to February 2007 by using NCEP-1 data. To maintain temporal homogeneity, the

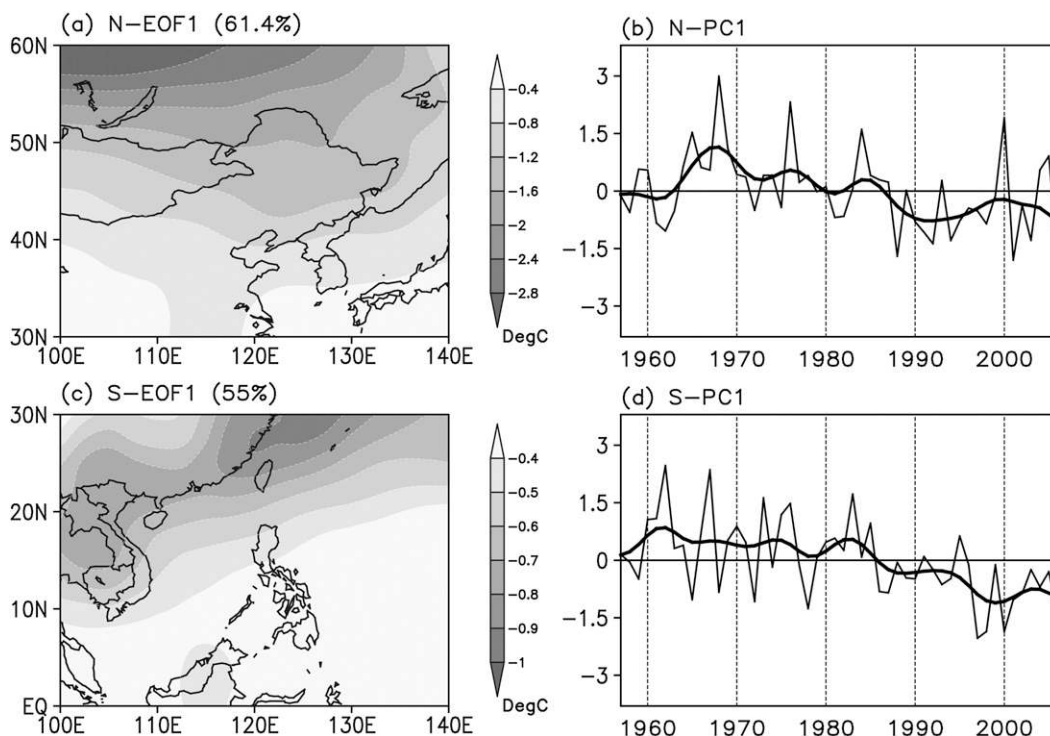


FIG. 2. (a) Spatial pattern and (b) the corresponding time coefficient of the first EOF modes of the winter mean 2-m air temperature ($^{\circ}\text{C}$) in the northern EAWM domain (30° – 60°N , 100° – 140°E). (c),(d) As (a),(b), but for the southern EAWM domain (0° – 30°N , 100° – 140°E). The numbers in the brackets indicate fractional variance of the EOF modes. The bold lines in (b) and (d) represent the decadal component, which describes the variation on a time scale >8 yr.

2002–07 NCEP-1 data were adjusted by removing the climatological difference between the ERA-40 and NCEP-1 datasets.

The sea surface temperature (SST) data were derived from the extended reconstructed SST version 2 (ERSST V2) data (Smith and Reynolds 2004). The precipitation data used in this study were obtained from the monthly global land precipitation [precipitation reconstruction by gauge observations over land (PREC/L)] data gridded at $1.0^{\circ} \times 1.0^{\circ}$ resolution (Chen et al. 2002). The Northern Hemisphere snow data were taken from the NCEP/Climate Prediction Center records (online at <http://www.cpc.noaa.gov/data/snow/>).

3. Distinct northern and southern modes of EAWM variability

To reveal latitudinal differences, we first performed EOF analysis of the 2-m air temperature (T_s) over the northern domain (30° – 60°N , 100° – 140°E) and the southern domain (0° – 30°N , 100° – 140°E) separately. The EOF analysis was carried out by constructing an area-weighted covariance matrix. In an area-weighted covariance matrix, a $\cos\Phi$ weighting was applied to the analyzed variable, taking into account of the convergence of the meridians with latitude, where Φ refers to latitudes.

The spatial patterns and the corresponding principal components (PCs) are presented in Fig. 2. The two leading modes derived for the northern and southern EA account for 61.4% and 55.0% of the total variance in the corresponding northern and southern domains, respectively. Both modes show a monosign pattern, with maximum loading located in the northern part of the domain and amplitude decreasing southward (Figs. 2a,c). However, they are independent of each other, as evidenced by the insignificant correlation between the two PCs (-0.06 ; see Figs. 2b,d).

It is of interest to see whether these latitudinal differences can be detected by the EOF analysis over the entire EAWM domain (0° – 60°N , 100° – 140°E). The resultant whole-domain EOF1 and EOF2 are presented in Fig. 3. The two modes explain 55.0% and 18.7% of the total variance, respectively. Analysis of the eigenvalues suggests that the two leading modes are significantly distinguished from each other and from the rest of the eigenvectors in terms of sampling error above the 95% confidence level (North et al. 1982). The spatial pattern of EOF1 shows the largest negative anomaly around 60°N , and the amplitude decreases southward, signifying a cold-air pathway intruding into EA from due north (Fig. 3a). The spatial pattern of EOF2 displays a maximum

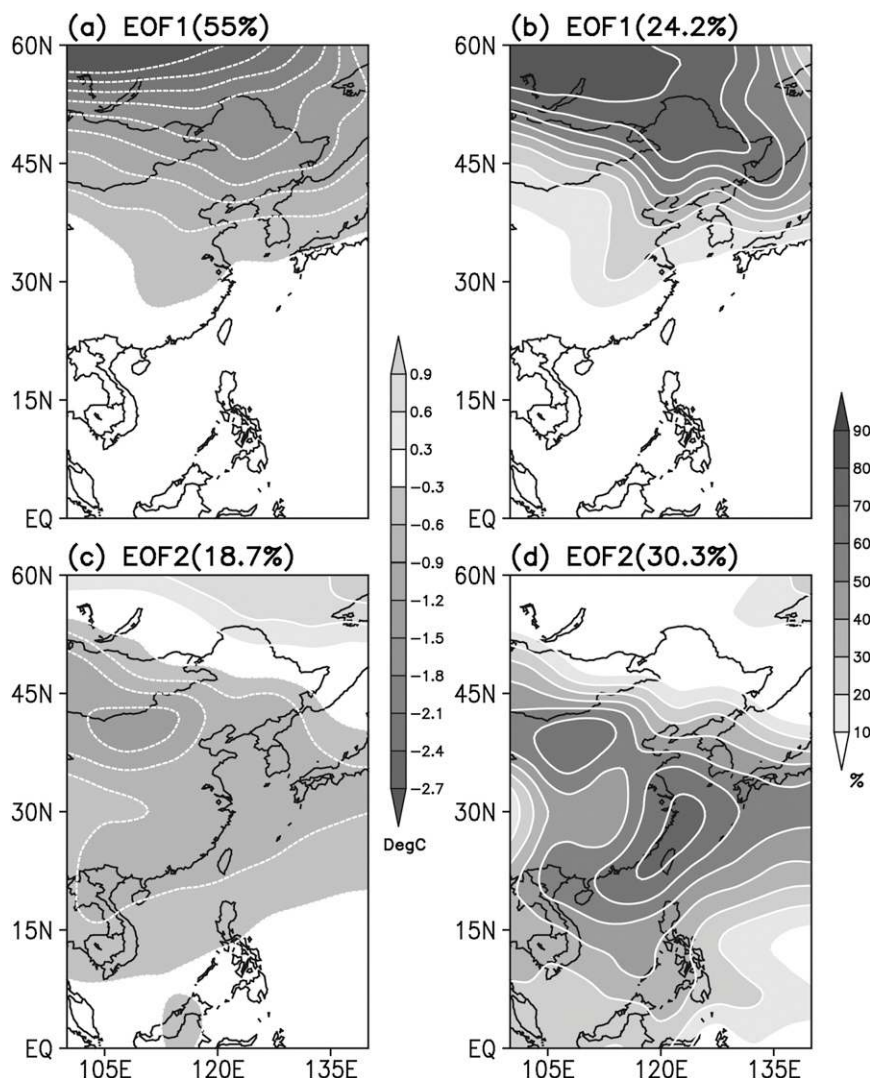


FIG. 3. (a) Spatial patterns ($^{\circ}\text{C}$) and (b) the percentage (normalized) variance of the first EOF mode of the winter mean 2-m air temperature in the entire EAWM domain. (c), (d) As (a), (b), but for the second EOF mode. The numbers in parentheses on the top of left panels denote the contribution to the total variances, whereas those on the right panels denote to the total normalized variances.

cooling in southern Inner Mongolia, and the major negative anomalies extend first southeastward from northwest Mongolia to the east coast of China, and then turn southwestward toward the South China Sea and Indochina peninsula (Fig. 3c).

Note that the EOF analysis here was conducted by constructing a covariance matrix. Thus, the derived spatial patterns in Figs. 3a,b depict distribution of the Ts anomalies with actual amplitudes. Because the total temperature variance decreases equatorward, the southern mode EOF2 accounts for only 18.7% of the total variance over the entire domain. However, from a seasonal prediction point of view, it is more useful to examine

the percentage variance, which is defined as the local variance normalized by the total variance at each grid point. The percentage variance distributions are shown in Figs. 3b,d, which indicate that EOF1 accounts for 50%–80% of the local percentage variance in the region north of 40°N , whereas EOF2 explains the majority (40%–80%) of the local percentage variance in the region between 10° and 40°N . Therefore, the two modes are complementary in describing local percentage variances. By averaging over the entire domain, EOF1 and EOF2 account for 24.2% and 30.3% of the total percentage variance, respectively. Thus, in terms of its contribution to the local variability, EOF2 is slightly more

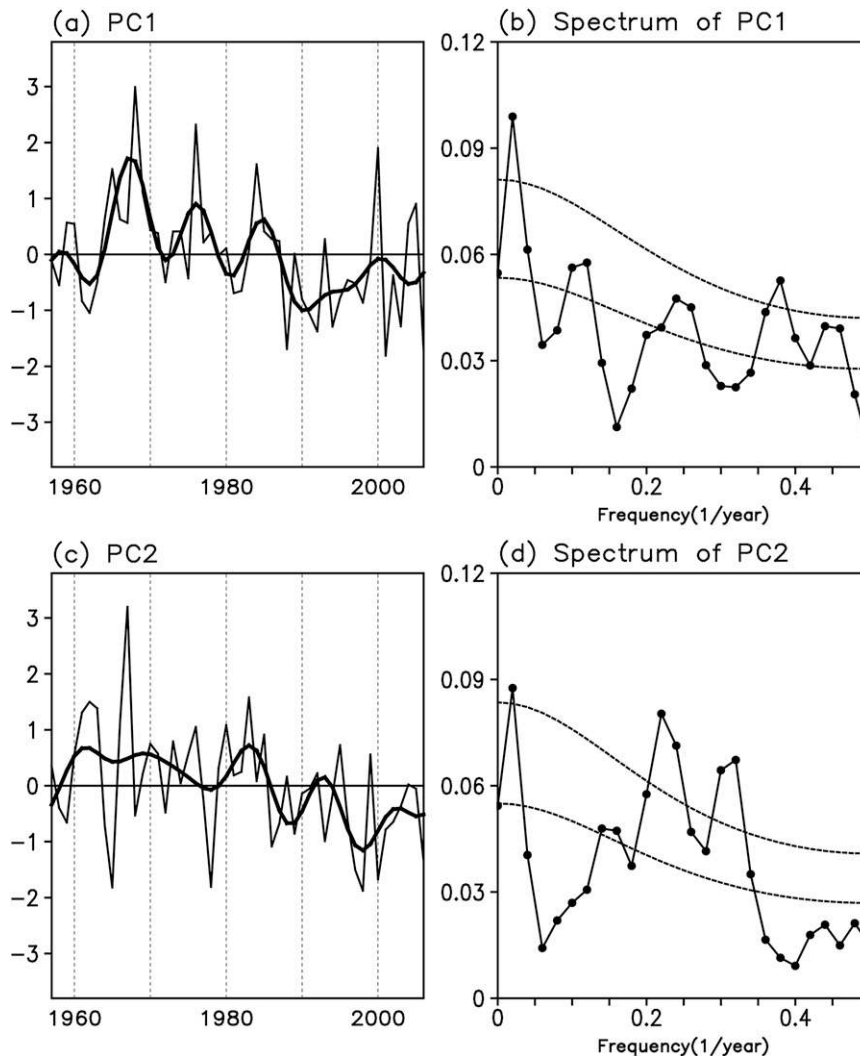


FIG. 4. Principal component (PC) of the (a) first and (c) second EOF modes for the winter mean 2-m air temperature in the entire EAWM domain. (b),(d) Corresponding power spectrum of the first and second EOF modes. The bold lines in (a) and (c) represent the decadal components, which describe the variations on time scales $> \text{yr}$.

important than EOF1. Over the region of 10° – 60°N , 100° – 140°E , the two leading modes together explain about 65% of the total fractional variance (calculated based on Figs. 3b,d).

Figure 4 displays the temporal behavior of the two modes, PC1 and PC2. Both PC1 and PC2 show a sharp decrease in the mid-1980s over the past 50 yr (Figs. 4a,c), which implies an abrupt transition from a cold phase to a warm phase if the corresponding spatial patterns reverse their signs. The spectra of both PC1 and PC2 exhibit two time scales of variability: IA and ID (Figs. 4b,d). The ID peaks are centered around 40 yr for both modes. However, on the IA time scale, PC1 has a significant peak at 2.6 yr, whereas PC2 has two significant peaks at 3 and

5 yr. The results suggest that the two PCs may have coherent ID variation, but their IA variations are different.

Obviously, in the extratropical EA, the spatial pattern of EOF1 resembles that of the leading mode in the northern EA (Fig. 2a); in the tropical EA, the EOF2 pattern represents the leading mode in the southern EA (Fig. 2c). Further, PC1 is highly correlated with the PC of the northern domain mode (Fig. 2b), having a correlation coefficient of 0.99 for the period of 1957–2006; similarly, the correlation coefficient between PC2 and the PC1 of the southern domain mode is 0.89.

It is important to point out that the two modes derived from analysis of the EA air temperature represent the temperature variability beyond the EA. As

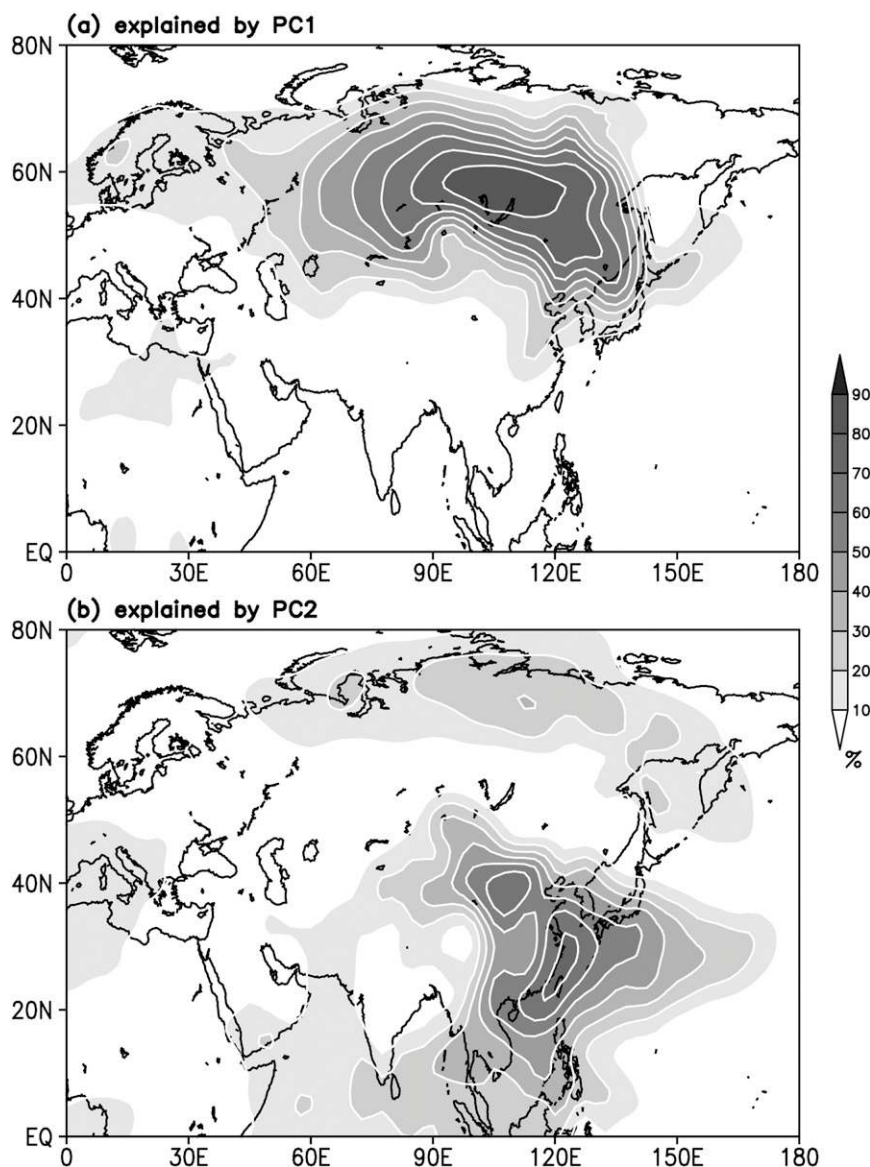


FIG. 5. Distribution of the percentage variances of the winter mean 2-m air temperature explained by (a) PC1 and (2) PC2, which are obtained from EOF analysis of the East Asian winter mean temperature.

shown in Fig. 5, the surface air temperature variations associated with the PC1 and PC2 account for not only the majority of the total percentage variance over the EA, but also over all of Asia. The northern and southern modes of the EAWM dominate, respectively, the temperature variability north and south of 40°N in a broad longitudinal range between 60° and 150°E, except for India, which is shadowed by the Tibetan Plateau. It is clear that the two modes derived from the EAWM domain capture the winter temperature variability for nearly all of Asia. Thus, the northern and southern modes are robust and insensitive to the

analysis domains. In the next section, one will see that the two modes not only depict temperature variations but also describe the variations of the Asian winter monsoon circulation system.

4. Contrasting dynamic structures of the northern and southern modes

a. Planetary-scale circulation anomalies associated with PC1 and PC2

Figures 6b,c show the anomalous surface circulation regressed with reference to PC1 and PC2 along with the

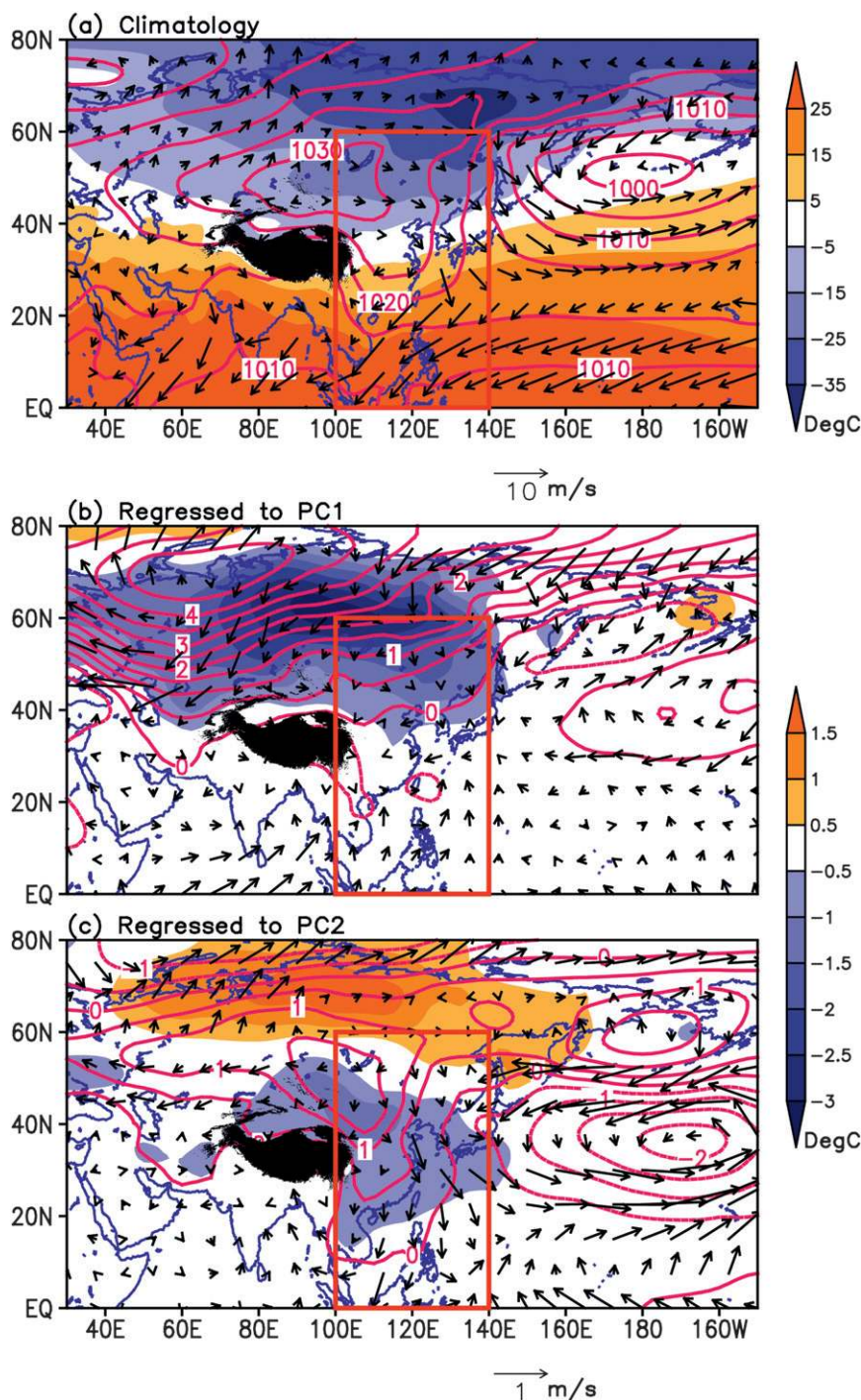


FIG. 6. SLP (contours, hPa), Ts (color shadings, °C), and surface winds (vectors, m s⁻¹) for (a) climatological winter mean and anomalies regressed with reference to (b) PC1 and (c) PC2.

climatology (Fig. 6a). For the northern mode, a gigantic anomalous high sea level pressure (SLP) occupies the entire northern Eurasian continent, with a major ridge extending southward along the Ural Mountain range and a minor ridge extending southeastward toward

northeastern China (Fig. 6b). The anomalous coldest surface air is located in western and central Siberia, south of the climatological cold dome. The northerly surface winds prevail in the northern EA, which advect cold air southward from due north. This pattern reflects the frequent

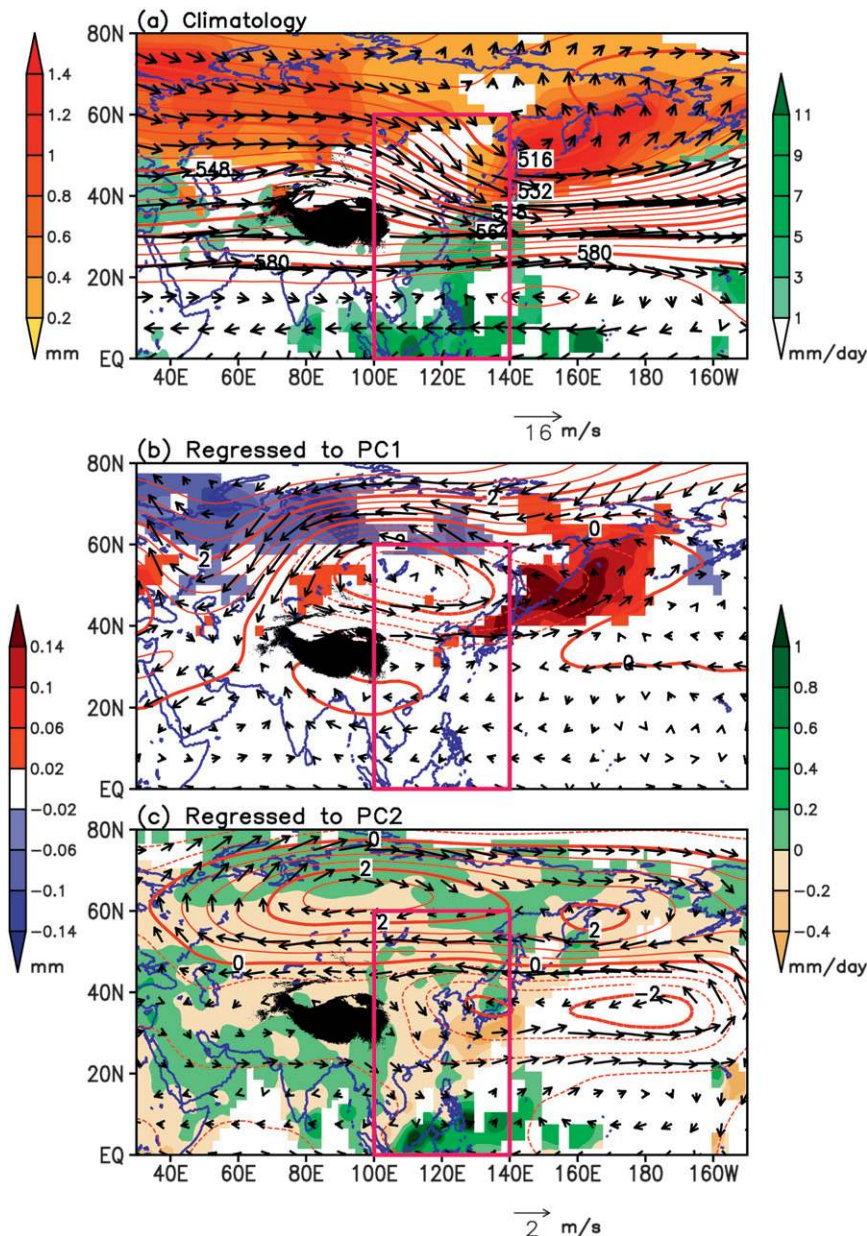


FIG. 7. The 500-hPa geopotential height (contours, 10 gpm), winds (vectors, m s^{-1}), precipitation rate (green–brown shadings, mm day^{-1}), and snowfall (blue–red shadings, mm) for (a) climatological winter mean, and anomalies regressed with reference to (b) PC1 and (c) PC2.

occurrence of a “northern pathway” of the cold-air outbreak from central Siberia to northern EA. However, the northerlies associated with the northern mode have little impact south of 30°N in East Asia. Over the Eurasian continent, the southern mode notably differs from the northern mode. A salient positive SLP anomaly center is seen over Mongolia, rather than the northern Ural Mountain. A prominent SLP ridge extends from Mongolia southward along the eastern flank of the Tibetan Plateau

to the South China Sea (Fig. 6c). This pattern reflects a route of cold-air intrusion along the eastern flank of the Tibetan Plateau via a “northwest pathway” from Mongolia to Southeast Asia. The large zonal gradient between the anomalous EA continent high and the subtropical North Pacific low implies strong anomalous northerlies over EA from 50°N all the way down to the equatorial region. Cold surface air temperature anomalies are found over northern and eastern China, Korea, Japan, the East

China Sea, and the South China Sea, while warm anomalies appear over northern Russia, primarily north of 50°N.

Figure 7 compares the anomalous large-scale circulations at midtroposphere that are associated with the northern and southern modes along with the climatology (Fig. 7a). For the northern mode, a strong low pressure anomaly center is located at Lake Baikal (55°N, 110°E) above the cold air mass, which is consistent with the thermal wind rule (Fig. 7b). Because the EA trough tilts southwestward from the Okhotsk Sea (60°N, 150°E) to the east coast of China (30°N, 120°E; see Fig. 7a), the anomalous low over Lake Baikal implies a westward shift of the EA major trough, which favors a cold-air outbreak from central Siberia toward northern China. Excessive snowfall is seen to the east of the 500-hPa anomalous low over the northwestern North Pacific, while a reduced snowfall is observed over the polar region in association with easterly anomalies (Fig. 7b). The pronounced circulation anomalies associated with the northern mode are basically located north of 40°N and exhibit a barotropic structure, except over the source region of the cold air (Siberia and Mongolia). On the other hand, for the southern mode, a huge elongated anticyclonic anomaly covers all of high-latitude Russia and the northern North Pacific (Fig. 7c), resulting from the anomalous warm air accumulating in the atmospheric column (Fig. 6c). An eminent barotropic low pressure anomaly is centered over the subtropical North Pacific (around 35°N, 170°W), exerting a notable forcing on the EAWM. An increase in rainfall is observed over the southern South China Sea and Philippines, indicating a linkage between the southern mode and equatorial convections.

Overall, the circulation anomalies associated with the northern and southern modes may be viewed as departures from the climatological norm, but the departures are in opposite directions. The northern mode tends to shift the SMH northwestward and the Aleutian low northward, while the southern mode shifts the SMH southeastward and the Aleutian low southwestward (Fig. 6). In the midtroposphere, the northern mode represents a northwestward shift of the EA major trough with a negative anomaly center near Lake Baikal, whereas the southern mode tends to shift the EA major trough southeastward with negative anomalies in the East China Sea and subtropical western North Pacific (Fig. 7). Thus, the two temperature modes well reflect the anomalous circulation variations.

b. Circulation indices for the northern and southern modes of EAWM

To objectively quantify the IA-to-ID variability and to facilitate understanding the influences of local and

remote forcing on the two leading modes, it is helpful to pinpoint the most sensitive circulation variability centers for the two leading modes. Analysis of the simultaneous correlations between the two PCs and the variations in the EAWM circulation systems helped to identify the most sensitive regions. Because the correlation maps are similar to (albeit not the same as) the regression maps shown in Figs. 6 and 7, for brevity's sake we do not show these similar maps here, but only highlight the results in Fig. 8.

Figure 8 shows the key regions in the 500-hPa geopotential height (H500) and SLP field that are best correlated with the two PCs. At 500 hPa, the northern mode can be best measured by the anomalous H500 anomaly over the Lake Baikal region (40°–60°N, 90°–130°E) with a correlation coefficient of 0.90 (Fig. 8a), while the southern mode is best measured by the H500 anomaly over the southern part of the EA trough (EAT; 20°–40°N, 110°–130°E) with a correlation coefficient of -0.77 (Fig. 8a). This means that a cold northern mode is characterized by a westward shift of the climatological EA trough, while a cold southern mode is signified by a deepening EA trough (and an associated acceleration southward shift of the westerly jet stream). In terms of SLP, the northern mode may be gauged by the SLP anomaly over central Siberia (55°–75°N, 90°–120°E), with a correlation coefficient of 0.80, while the southern mode may be measured by the SLP difference between Mongolia (40°–55°N, 90°–120°E) and the subtropical western North Pacific (SWNP; 20°–40°N, 150°–180°E)— $\text{SLP}(\text{MH}) - \text{SLP}(\text{SWNP})$ —with a correlation coefficient of 0.79 (Fig. 8b). This result implies that a strengthening central Siberian high corresponds to a cold northern mode, whereas a strengthening pressure gradient between the Mongolia and the SWNP corresponds to a cold southern mode. Note that both modes are also related to variations in the Aleutian low, but the corresponding correlation coefficients are significantly lower than those associated with the SMH and EA major trough.

Based on the results in Fig. 8, we propose that the variability of the EAWM can be measured by a pair of circulation indices that characterize the strength of the northern and southern modes, respectively. The northern mode index is the 500-hPa geopotential height anomaly averaged over Lake Baikal (40°–60°N, 90°–130°E); the southern mode index is the SLP difference between Mongolia and the subtropical WNP (Fig. 8b). Combined indices were also constructed in an attempt to quantify both principal modes using a single index. The H500 averaged over 30°–50°N, 110°–130°E correlates with both the northern (-0.53) and southern (-0.61) modes reasonably well. The SLP averaged over 40°–65°N, 90°–120°E seems to be a reasonable index for measuring both the northern (0.51) and southern (0.64) modes. We have

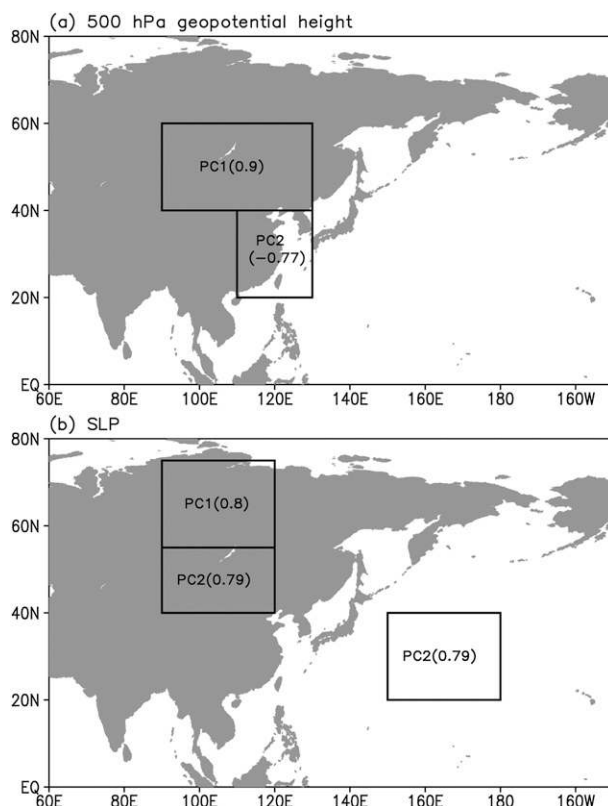


FIG. 8. Geographic regions that define the circulation indicators for the northern and southern modes at (a) 500-hPa geopotential height and (b) SLP fields. The numbers in the parentheses indicate the correlation coefficients between the corresponding PC and the area-averaged index (SLP or 500-hPa geopotential height). For PC2, the SLP index is defined as the SLP difference between Mongolia and the SWNP region [$\text{SLP}(\text{MH}) - \text{SLP}(\text{SWNP})$].

examined 10 existing EAWM circulation indices, and 9 indices basically describe the southern modes. Only one index (Guo 1983) describes both modes equally well (0.58, 0.56). This index is defined by SLP differences from 20° to 50°N between 110° and 160°E.

5. The differences between the interannual and interdecadal variation

The spectra showed in Figs. 4b,d suggest that both the northern and southern modes involve two time scales: the IA and ID. To investigate the origins of the IA and ID variability, we first identified structural differences between the IA and ID components. For this purpose, we decomposed PC1 and PC2 into IA and ID components. The IA component contains all Fourier harmonics that have periods of less than 8 yr, while the ID component contains all Fourier harmonics that have periods longer than 8 yr, including decadal variations. The ID components of PC1 and PC2 are shown by the thick solid curves in Fig. 4. Computation of the variances

carried by the two components indicates that for both PC1 and PC2, the IA component accounts for about two-thirds of the total variance, while the ID component explains about one-third thereof. Given the dominance of the IA component, one would anticipate that the structures of the IA component may be similar to those of the corresponding PCs. On the other hand, given the different time scales, the IA and ID components for the same mode may have different circulation anomalies.

Figure 9 compares the circulation anomalies associated with the IA and ID component of the northern mode. As anticipated, the structure of PC1(IA) shown in Figs. 9a,b closely resembles the structure of the northern mode (Figs. 6b and 7b). However, the structure associated with PC1(ID), while bearing an overall resemblance with that of PC1(IA), shows clear differences (Figs. 9c,d). The major difference is seen in the position of the 500-hPa anomalous low over north Asia: its center is located at Lake Baikal for the IA component but shifts to northeastern China for the ID component. Corresponding to the deepening EA trough in northeastern China, the surface anomalous high associated with the ID component also extends southward from Lake Baikal to central China.

Figure 10 compares the circulation anomalies associated with the IA and ID components of PC2. Again, the structure of PC2(IA) shown in Figs. 10a,b bears close resemblance to the structure of the southern mode (Figs. 6c and 7c). Note that the structure associated with PC2(ID) is completely different from its IA counterpart, but it resembles that of PC1(ID). In other words, the ID components of PC1 and PC2 share some common structural characteristics. This is particularly evident in the SLP anomalies over the Asian continent. The 500-hPa circulation anomalies also show similarities between the two ID components, although to a less degree. Over North America, the North Atlantic, and Europe, the circulation anomalies associated with the two ID components are also comparable; in contrast, those associated with the two IA components tend to be out of phase (figures not shown). The time coefficients of PC1(ID) and PC2(ID) have a correlation coefficient of 0.5, exceeding the 95% confidence level. These facts indicate that PC1 and PC2 have a somewhat similar spatiotemporal structure on the ID time scale, but they are remarkably discrete on the IA time scale. This has important implications in interpreting the origins of the two leading PCs.

6. Precursors of the northern and southern modes

To reveal possible sources of predictability, we search for precursors of the two principal modes in SST and snow

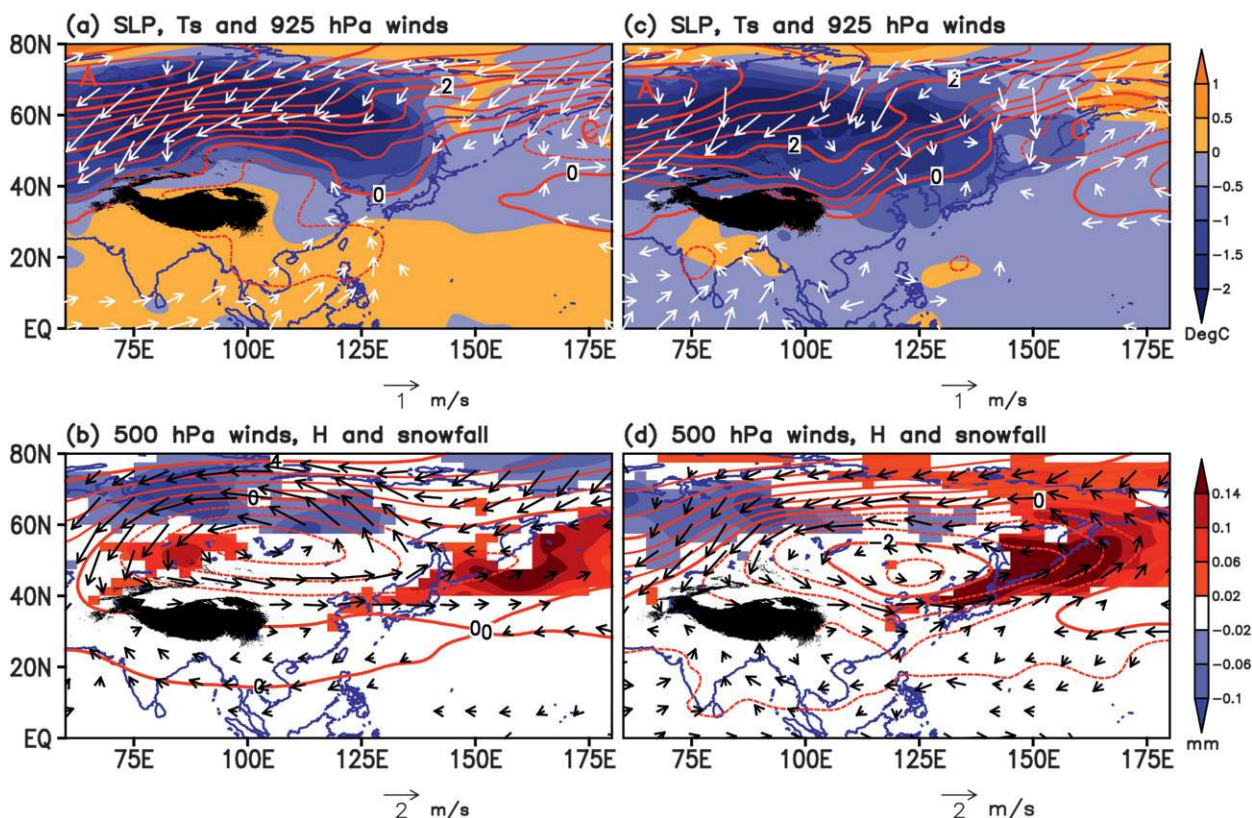


FIG. 9. Comparison of the Dec–Feb circulation anomalies regressed with reference to (a) the IA component and (b) the ID component of PC1. (top) SLP, Ts, and 925-hPa winds. (bottom) The 500-hPa geopotential height, winds, and snowfall. The contours and shadings have the same units that are used in Figs. 6b and 7b.

cover anomalies during the previous autumn. Considering the different structures of the IA and ID components, our analyses will apply to the IA and ID components, separately.

a. Interannual variations

The IA component of the northern mode has no significant correlation with the tropical SST anomaly (SSTA) in the prior autumn, suggesting its independence from ENSO. However, the occurrence of the northern mode is preceded by pronounced large-scale snow cover anomalies in the southern Siberia–Mongolia region during the preceding autumn (Fig. 11a). The IA component of the southern mode, on the other hand, has an anomalously negative correlation with autumn SSTA in a large area extending from the equatorial eastern Pacific to the date line, which signifies developing La Niña (Fig. 11b). Thus, the development of La Niña in autumn is an antecedent anomalous boundary condition for the occurrence of a strengthened winter monsoon over tropical and subtropical East Asia (the southern mode). Likewise, the development of El Niño preludes a weakened tropical–subtropical EAWM. In addition to the relationship with

La Niña–El Niño, the occurrence of a high PC2 is also preceded by reduced snow cover over northeastern Siberia (Fig. 11b).

b. Interdecadal variations

Figures 11c,d present correlations between SST in the previous autumn and the ID components of the two PCs. The correlation patterns associated with PC1(ID) and PC2(ID) bear an overall similarity, except that the SSTA associated with PC2(ID) displays a stronger amplitude and a more coherent spatial pattern. During the autumn prior to a weakened EAWM on the ID time scale, pronounced warming is seen in the tropical Indian Ocean and Maritime Continent and in the subtropical–midlatitude North Atlantic (Figs. 11c,d). This pattern is somewhat similar to, but not the same as, that associated with the global warming trend [Intergovernmental Panel on Climate Change (IPCC) Fourth Assessment Report (AR4)]. The major precursors for ID variations in the northern and southern modes in the preceding autumn are the SST anomalies over the North Atlantic and the tropical Indian Ocean–Maritime Continent.

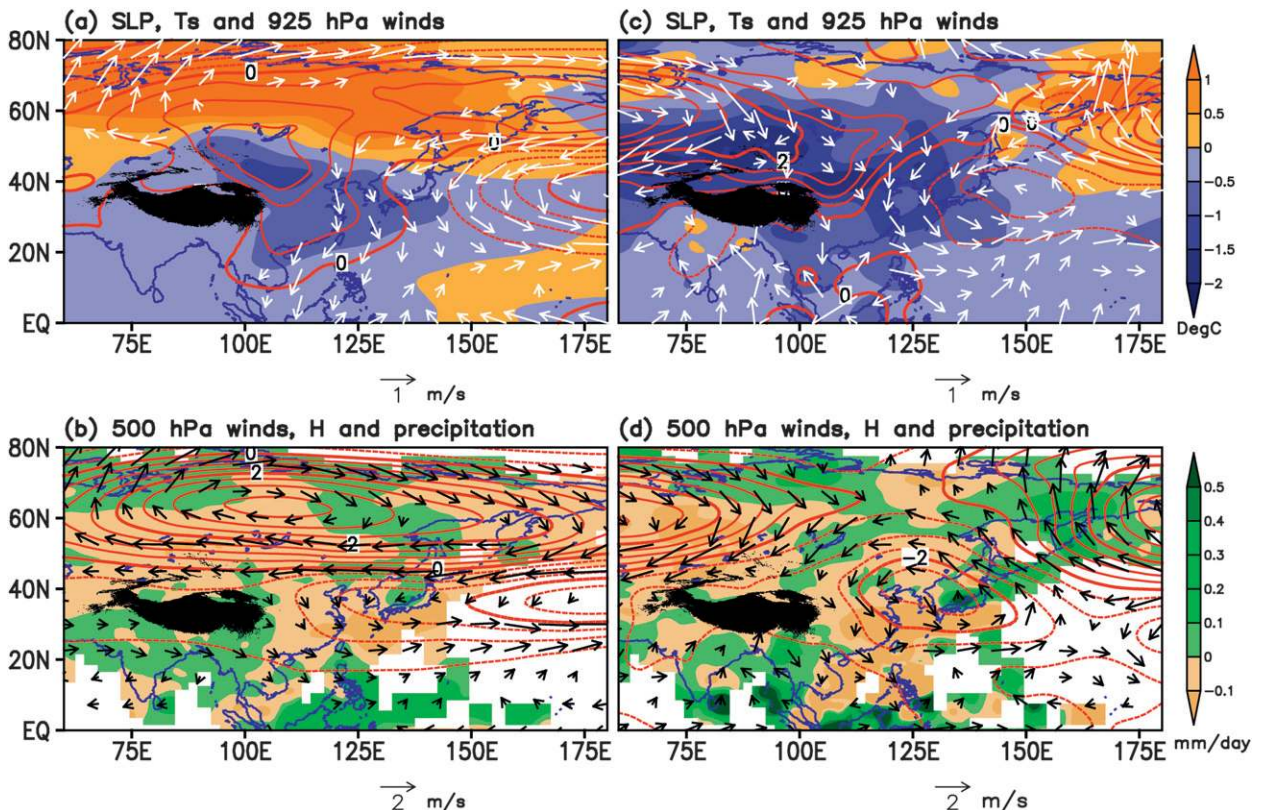


FIG. 10. As in Fig. 9, but for regressed anomalies against the IA and ID components of PC2. The contours and shadings have the same units that are used in Figs. 6c and 7c.

c. Predictors for the southern and northern modes

The boxed regions shown in Fig. 11 indicate the key geographic regions that are used to define the SST and snow cover predictors during the preceding autumn. Table 1 presents the correlation coefficients between the two PCs and the corresponding precursors in the preceding autumn. For the northern mode (PC1), the correlation coefficient with the southern Siberian snow cover averaged over 45° – 60° N, 70° – 140° E is 0.55 for the period of 1973–2005 (Table 1). For the southern mode, the correlation coefficient between the autumn Niño-3 SST and PC2 is -0.35 for the period of 1957–2006. The PC2 is also preceded by reduced snow cover over northeastern Siberia (60° – 70° N, 130° – 180° E), with a significant correlation coefficient of -0.39 (Table 1). The autumn SSTA over the North Atlantic (0° – 50° N, 60° – 10° W) and the tropical Indian Ocean–Maritime Continent (15° S– 15° N, 40° – 140° E) are significant predictors for both the northern and southern modes. However, these significant correlations come primarily from their ID components (Table 1). On the ID time scale, the variation in the autumn SSTA over the North Atlantic (0° – 50° N, 60° – 10° W) and the SSTA over the tropical Indian Ocean–Maritime Continent (15° S– 15° N, 40° – 140° E)

are good predictors for the ID variations in the southern mode; their correlation coefficients are -0.82 and -0.77 , respectively. Similarly, these SSTA are also meaningful indicators for the ID variation in the northern mode; the correlation coefficients are -0.52 and -0.49 , respectively (Table 1). Note that the ID components have persistence and the correlations computed using ID components have artificial skills resulting from data filtering. Therefore, when examining the statistical significance of the correlations between two ID components, the degrees of freedom must be reassessed using the method proposed by Chen (1982). For the 50-yr period, the degree of freedom is reduced to about 14. For the given confidence level of 0.95, a significant correlation should be greater than 0.5. Therefore, the above-mentioned correlations are statistically significant, except for the correlation between the Indian Ocean ID SSTA and the PC1(ID).

7. Origins of the EAWM's interannual-to-interdecadal variability

In this section, we discuss the physical processes through which the lower boundary forcing affects the EA winter monsoon variability.

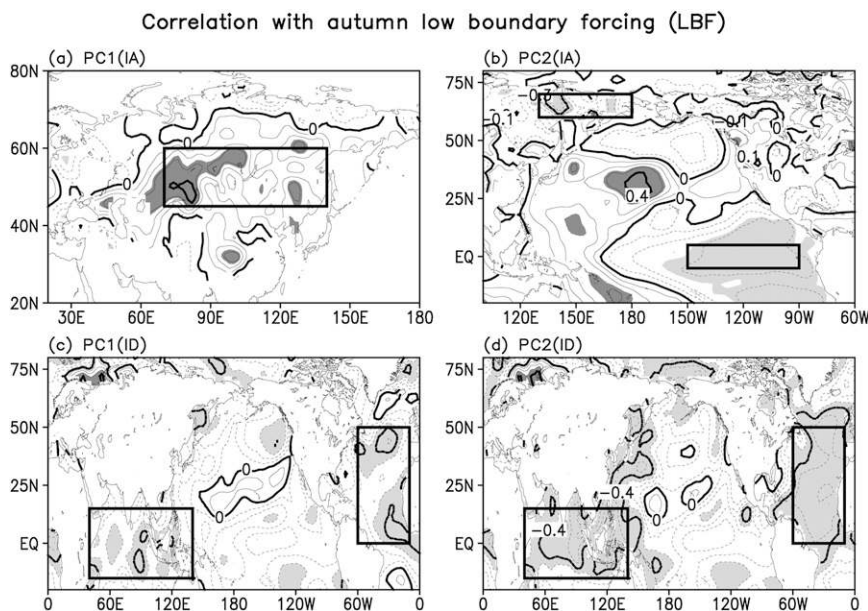


FIG. 11. Correlation coefficient map between the low boundary forcing anomalies (anomalous SST over ocean and snow cover over land) in the previous autumn and the IA-ID components of PCs. (a) PC1(IA), (b) PC2(IA), (c) PC1(ID), and (d) PC2(ID). The contour interval is 0.1. The dark (light) shaded regions represent positive (negative) correlation coefficients exceeding 95% confidence level.

a. Snow covers

The autumn snow cover and the EAWM relationships in specific regions and on specific years or time scales have been previously recognized (e.g., Watanabe and Nitta 1999; Clark and Serreze 2000; Gong et al. 2003; Jhun and Lee 2004). The new finding here is that the snow cover has a differing relationship with the two principal modes of the EAWM: a cold winter in northern EA is preceded by excessive snow cover over southern Siberia (45° – 60° N, 70° – 140° E), while a strong winter monsoon over southern EA is preceded by reduced snow cover over northeastern Siberia (60° – 70° N, 130° – 180° E).

The increased autumn snow cover over southern Siberia–Mongolia can reduce solar radiation flux received by the surface, favoring cold air mass accumulation in the boundary layer during the autumn and the ensuing winter. As a result, the 500-hPa geopotential

height in the vicinity of Lake Baikal would decrease, which implies a cold northern mode (Fig. 8). This mechanism corroborates the previous numerical experiment results, which show that extensive snow cover over some specific regions of Siberia can enhance the SMH, Aleutian low, and the East Asian jet, thus cooling the lower troposphere (e.g., Kumar and Yang 2003; Jhun and Lee 2004). The reduced snow cover over northeastern Siberia is expected to result in local warmer-than-normal climate and positive pressure anomalies in the 500 hPa, which are consistent with observations (Figs. 6c and 7c). The impact of the northeastern Siberian snow covers on the EAWM remains to be tested with atmospheric general circulation models.

b. ENSO

The relationship between the EAWM and ENSO has been noted previously (e.g., Zhang et al. 1996; Tomita

TABLE 1. Correlation coefficients between the two leading PCs and corresponding predictors in the preceding autumn. Statistical significant values at 95% confidence level are in bold.

Predictors	PC1	PC1(ID)	PC1(IA)	PC2	PC2(ID)	PC2(IA)
Southern Siberian snow cover (45° – 60° N, 70° – 140° E)	0.55	0.30	0.46	0.15	0.07	0.13
Northeast Siberian snow cover (60° – 70° N, 130° – 180° E)	0.09	0.01	0.10	−0.39	−0.45	0.16
Niño-3 SSTA	0.02	0.10	0.06	−0.35	0.10	−0.35
ID North Atlantic SSTA (0° – 50° N, 60° – 10° W)	−0.34	−0.52	0.00	−0.42	−0.82	0.00
ID SSTA in tropical Indian Ocean–Maritime Continent (15° S– 15° N, 0° – 140° E)	−0.31	0.49	0.07	−0.28	−0.77	0.05

and Yasunari 1996; Ji et al. 1997; Hamada et al. 2002; Chang et al. 2004). The new finding here is that only the southern mode (PC2) is affected by ENSO, while the northern mode is ENSO independent. How can a developing El Niño (La Niña) weaken (enhance) the EAWM in the southern domain? Taking El Niño as an example, a critical system that weakens the southern EAWM is the anomalous Philippine Sea anticyclone (PSAC), because the anomalous southwesterlies to the west of the PSAC center reduces the northeasterly winter monsoon over southern EA (i.e., central-southern China, the East and South China Sea). During the El Niño development year, the PSAC anomaly is established over the northern Philippines in late September and October in an abrupt manner (Wang and Zhang 2002). Therefore, a key question is as follows: Why and how does the PSAC anomaly become established during El Niño in autumn? The onset of PSAC concurs with a swing of the intraseasonal oscillation from a low to a high pressure phase (Wang and Zhang 2002) and the associated synoptic development is similar to those accompanying cold-air surges over East Asia (Lau and Nath 2006). During the PSAC formation the remote El Niño forcing, the tropical–extratropical interaction, and the local monsoon–ocean interaction play critical roles (Wang and Zhang 2002). In addition, Watanabe and Jin (2003) suggested that the effect of the Indian Ocean may also contribute to the establishment of the PSAC.

c. Interdecadal variation in North Atlantic and tropical Indian Ocean SST

Beyond the IA time scale the SST anomalies over the North Atlantic and the tropical Indian Ocean–Maritime Continent prelude the anomalous winter monsoon in the entire EAWM domain, especially for southern EA (Figs. 11c,d). It is found that the North Atlantic and tropical Indian Ocean SST anomalies in autumn can lead to a deepening of the southern part of the EA trough, indicating an enhanced southern mode (Fig. 8a). However, the precise processes by which the North Atlantic and the tropical Indian Ocean affect the EA major trough in the winter remain elusive and deserve further numerical study.

d. Other modes of climate variability

Some previous studies have attributed EAWM variability to other major modes of climate variability, including either the AO or NAM (Gong et al. 2001; Wu and Wang 2002; Li and Wang 2003; Jeong and Ho 2005) and NAO (Li and Bates 2007; Panagiotopoulos et al.

2005). Although the overall circulation anomaly associated with the northern mode resembles a negative phase of the NAM/AO, the seasonal variation of the AO/NAM itself is primarily associated with atmospheric internal dynamics and is thereby chaotic (e.g., Robertson et al. 2000; Baldwin 2001; Feldstein 2000). It is thus difficult to regard the AO/NAM as causing EAWM variability. Similar to NAM, the reproducibility of NAO is low, even with prescribed climate forcing and historical sea surface conditions (Scaife et al. 2008). On the ID time scale, however, NAO may be partially predictable because of its coupling with the changes in the thermohaline circulation through North Atlantic Deep Water formation (Mikolajewicz and Maier-Reimer 1990; Timmermann et al. 1998). Thus, the North Atlantic SSTA and NAO may potentially provide a source of predictability for the ID variation in the EAWM.

8. Concluding remarks

This study attempts to unveil the causes of interannual (IA)-to-interdecadal (ID) variability for the entire EAWM system using observed data over the past 50 yr (1957–2006). Analysis of 2-m air temperature offers a new perspective on the climate variability and predictability of the EAWM. The major findings are summarized as follows:

- The IA–ID variation in surface air temperature over EA (0° – 60° N, 100° – 140° E) is dominated by two distinct principal modes: the northern and southern mode. These two modes depict temperature variability in the northern and southern EA and reflect different cold-air pathways intruding into EA from due north and northwest, respectively. An accurate prediction of these two modes will be capable of capturing about 74% of the total variance of the surface air temperature over EA. The northern mode has been largely overlooked in the past because a majority of the EAWM indices describe the southern mode only. We have shown that the northern and southern modes are complimentary and equally important in terms of seasonal prediction.
- The northern and southern modes exhibit distinguished circulation structures. The cold northern mode is characterized by a deepening 500-hPa geopotential height to the west of the EA trough near Lake Baikal (40° – 60° N, 90° – 130° E) and an enhanced SLP in central Siberia (55° – 75° N, 90° – 120° E; Fig. 8). In contrast, the cold southern mode features a deepening southern part of the EA trough (20° – 40° N, 110° – 130° E) and enhanced SLP gradients between Mongolia (40° – 55° N, 90° – 120° E) and the SWNP (20° – 40° N, 150° – 180° E). Two circulation indices have been designed to measure

the variations of the northern and southern modes, respectively.

- Both leading modes have an IA and ID component; the ID component accounts for about one-third of the total variance for both PC1 and PC2. The northern and southern modes exhibit distinctive spatiotemporal structures on the IA time scale, but share some common spatial and temporal characteristics in their ID variations.
- The two leading modes have different precursors on an IA time scale. A cold northern mode is preceded by excessive autumn snow cover over southern Siberia (45°–60°N, 70°–140°E), whereas the enhanced southern mode is preceded by the development of a La Niña episode and reduced snow cover over northeastern Siberia (60°–70°N, 130°–180°E).
- On an ID time scale, the major common precursors for both modes are the autumn SST anomalies over the North Atlantic and the tropical Indian Ocean–Maritime Continent. This is particularly evident for the southern mode (Table 1).

A bitter winter means both low temperature and enhanced northerlies. In China, Japan, and Korea, prediction of temperature anomalies usually receive most attention and the term “cold-air outbreaks” or “cold waves” are often used to describe the significant events of a strong EAWM (Ding and Sikka 2006; Chang et al. 2010). On the other hand, in the East China Sea and South China Sea the term “monsoonal surges” or “cold surges” focuses on the strong surface winds (Chang et al. 2006, 2010). These perceptions are consistent with the climatology in which strong monsoonal winds occur over the ocean and marginal seas (Fig. 6a). From this point of view, a cold southern mode corresponds better to a strong monsoonal wind than the northern mode. That explains why most existing studies of the EAWM focus on low-level winds. However, the northerly wind is consistent with temperature anomalies associated with both modes, and a new perspective gained from this study is that the northern and southern modes are complementary and are of nearly equal importance to the winter temperature variations over the EA and nearly the entire Asia.

Because the two modes account for 74% of the total variance in the winter mean 2-m air temperature over the entire EAWM domain (Fig. 3), accurate prediction of these two modes can capture a major portion of the surface air temperature anomalies. Because they also represent the temperature variability over the entire Asian continent (Fig. 5), study of the predictability of these two modes is also very important for understanding predictable dynamics of the Asian winter monsoon. In section 7, we have provided a detailed discussion to

stimulate further numerical and theoretical studies to better understand the predictable dynamics of the EAWM. In addition, the extent to which we can predict these empirical modes with dynamical models and with physically based empirical models is unclear but is currently under investigation.

Acknowledgments. The first two authors are supported by IPRC, which is in part sponsored by FRCGC/ JAMSTEC, NASA, and NOAA. Jian Liu and Bin Wang acknowledge the support of the National Natural Science Foundation of China (Grants 40672210 and 40871007). Zhiwei Wu, Jianping Li, and Tianjun Zhou acknowledge the support of the Special Research Program for Public Welfare (Meteorology) of China (Grant GYHY200906016), the National Basic Research Program “973” (Grant 2006CB403600), and the National Natural Science Foundation of China (Grant 40821092). C.-P. Chang acknowledges the support from the National Taiwan University, which is provided in part by National Science Council Grant NSC97-2111-M-002-017-MY3.

REFERENCES

- Baldwin, M. P., 2001: Annular modes in global daily surface pressure. *Geophys. Res. Lett.*, **28**, 4115–4118.
- Chan, J., and C. Li, 2004: The East Asia winter monsoon. *East Asian Monsoon*, C.-P. Chang, Ed., World Scientific, 54–106.
- Chang, C.-P., and K. M. Lau, 1980: Northeasterly surge and near equatorial disturbances over the winter MONEX area during December 1974. Part II: Planetary scale aspects. *Mon. Wea. Rev.*, **108**, 298–312.
- , and —, 1982: Short-term planetary-scale interaction over the tropics and midlatitudes during northern winter. Part I: Contrast between active and inactive periods. *Mon. Wea. Rev.*, **110**, 933–946.
- , J. E. Millard, and G. T. J. Chen, 1983: Gravitational character of cold surges during winter MONEX. *Mon. Wea. Rev.*, **111**, 293–307.
- , Z. Wang, J. Ju, and T. Li, 2004: On the relationship between western maritime continent monsoon rainfall and ENSO during northern winter. *J. Climate*, **17**, 665–672.
- , —, and H. Hendon, 2006: The Asian winter monsoon. *The Asian Monsoon*, B. Wang, Ed., Praxis, 89–127.
- , M.-M. Lu, and B. Wang, 2010: The East Asian winter monsoon. *The Global Monsoon System: Research and Forecast*, 2nd ed., C.-P. Chang et al., Eds., World Scientific, in press.
- Chen, M., P. Xie, J. E. Janowiak, and P. A. Arkin, 2002: Global land precipitation: A 50-yr monthly analysis based on gauge observations. *J. Hydrometeorol.*, **3**, 249–266.
- Chen, W., H. Graf, and R. H. Huang, 2000: The interannual variability of East Asian winter monsoon and its relation to the summer monsoon. *Adv. Atmos. Sci.*, **17**, 48–60.
- Chen, W. Y., 1982: Fluctuations in Northern Hemisphere 700 mb height field associated with southern oscillation. *Mon. Wea. Rev.*, **110**, 808–832.
- Clark, M. P., and M. C. Serreze, 2000: Effects of variations in East Asian snow cover on modulating atmospheric circulation over the North Pacific Ocean. *J. Climate*, **13**, 3700–3710.

- Compo, G. P., G. N. Kiladis, and P. J. Webster, 1999: The horizontal and vertical structure of east Asian winter monsoon pressure surges. *Quart. J. Roy. Meteor. Soc.*, **125**, 29–54.
- Cui, X., and Z. Sun, 1999: East Asian winter monsoon index and its variation analysis. *J. Nanjing Inst. Meteor.*, **22**, 321–325.
- Ding, Y. H., 1990: Buildup, air-mass transformation and propagating of Siberian high and its relations to cold surge in East Asia. *Meteor. Atmos. Phys.*, **44**, 281–292.
- , 1994: *Monsoons over China*. Kluwer Academic, 419 pp.
- , and T. N. Krishnamurti, 1987: Heat budget of the Siberian high and the winter monsoon. *Mon. Wea. Rev.*, **115**, 2428–2449.
- , and D. R. Sikka, 2006: Cold waves and cold surges. *The Asian Monsoon*, B. Wang, Ed., Praxis, 184–194.
- Feldstein, S. B., 2000: The timescale, power spectra, and climate noise properties of teleconnection patterns. *J. Climate*, **13**, 4430–4440.
- Gong, D.-Y., S.-W. Wang, and J.-H. Zhu, 2001: East Asian winter monsoon and Arctic Oscillation. *Geophys. Res. Lett.*, **28**, 2073–2076.
- Gong, G., D. Entekhabi, and J. Cohen, 2003: Modeled Northern Hemisphere winter climate response to realistic Siberian snow anomalies. *J. Climate*, **16**, 3917–3931.
- Guo, Q. Y., 1983: Relationship between the variations of East Asian winter monsoon and temperature anomalies in China. *Chin. J. Appl. Meteor.*, **5**, 218–225.
- Hamada, J.-I., M. Yamanaka, J. Matsumoto, S. Fukao, P. Winarso, and T. Sribimawati, 2002: Spatial and temporal variations of the rainy season over Indonesia and their link to ENSO. *J. Meteor. Soc. Japan*, **80**, 285–310.
- Jeong, J.-H., and C.-H. Ho, 2005: Changes in occurrence of cold surges over east Asia in association with Arctic Oscillation. *Geophys. Res. Lett.*, **32**, L14704, doi:10.1029/2005GL023024.
- Jhun, J.-G., and E.-J. Lee, 2004: A new East Asian winter monsoon index and associated characteristics of winter monsoon. *J. Climate*, **17**, 711–726.
- Ji, L. R., S. Shuqing, K. Arpe, and L. Bengtsson, 1997: Model study on the interannual variability of Asian winter monsoon. *Adv. Atmos. Sci.*, **14**, 1–22.
- Kalnay, E., and Coauthors, 1996: The NCEP/NCAR 40-Year Re-analysis Project. *Bull. Amer. Meteor. Soc.*, **77**, 437–471.
- Kumar, A., and F. Yang, 2003: Comparative influence of snow and SST variability on extratropical climate in northern winter. *J. Climate*, **16**, 2248–2261.
- Lau, K. M., and C.-P. Chang, 1987: Planetary scale aspects of winter monsoon and teleconnections. *Monsoon Meteorology*, C.-P. Chang and T. N. Krishnamurti, Eds., Oxford University Press, 161–202.
- Lau, N.-C., and M. J. Nath, 2006: ENSO modulation of the interannual and intraseasonal variability of the East Asian monsoon—A model study. *J. Climate*, **19**, 4508–4530.
- Li, J., and Q. Zeng, 2002: A unified monsoon index. *Geophys. Res. Lett.*, **29**, 1274, doi:10.1029/2001GL013874.
- , and J. X. L. Wang, 2003: A modified zonal index and its physical sense. *Geophys. Res. Lett.*, **30**, 1632, doi:10.1029/2003GL017441.
- Li, S., and G. Bates, 2007: Influence of the Atlantic multidecadal oscillation on the winter climate of East China. *Adv. Atmos. Sci.*, **24**, 126–135.
- Li, X. Z., 1955: A study of cold waves in East Asia. *Offprints of Scientific Works in Modern China—Meteorology (1919–1949)*, X. Z. Li, Ed., Science Press, 35–117.
- Lu, E., and J. Chan, 1999: A unified monsoon index for south China. *J. Climate*, **12**, 2375–2385.
- Matsumoto, J., 1992: The seasonal changes in Asian and Australian monsoon regions. *J. Meteor. Soc. Japan*, **70**, 257–273.
- Mikolajewicz, U., and E. Maier-Reimer, 1990: Internal secular variability in an ocean general circulation model. *Climate Dyn.*, **4**, 145–156.
- Murakami, T., 1987: Effects of the Tibetan Plateau. *Monsoon Meteorology*, C.-P. Zhang and T. N. Krishnamurti, Eds., Oxford University Press, 235–270.
- North, G. R., T. L. Bell, R. F. Cahalan, and F. J. Moeng, 1982: Sampling errors in the estimation of empirical orthogonal functions. *Mon. Wea. Rev.*, **110**, 699–706.
- Panagiotopoulos, F., M. Shahgedanova, A. Hannachi, and D. Stephenson, 2005: Observed trends and teleconnections of the Siberian High. *J. Climate*, **18**, 1411–1422.
- Robertson, A. W., C. R. Mechoso, and Y. J. Kim, 2000: The influence of Atlantic sea surface temperature anomalies on the North Atlantic oscillation. *J. Climate*, **13**, 122–138.
- Scaife, A. A., and Coauthors, 2008: The CLIVAR C20C Project: Selected 20th century climate events. *Climate Dyn.*, **33**, 603–614, doi:10.1007/s00382-008-0451-1.
- Smith, T. M., and R. W. Reynolds, 2004: Improved extended reconstruction of SST (1854–1997). *J. Climate*, **17**, 2466–2477.
- Tao, S. Y., 1957: A study of activities of cold airs in East Asian winter. *Handbook of Short-Term Forecast*, China Meteorological Administration, Eds., Meteorology Press, 60–92.
- Timmermann, A., M. Latif, R. Voss, and A. Groetzner, 1998: Northern Hemisphere interdecadal variability: A coupled air–sea mode. *J. Climate*, **11**, 1906–1931.
- Tomita, T., and T. Yasunari, 1996: Role of the northeast winter monsoon on the biennial oscillation of the ENSO/monsoon system. *J. Meteor. Soc. Japan*, **74**, 399–413.
- Uppala, S. M., and Coauthors, 2005: The ERA-40 Re-Analysis. *Quart. J. Roy. Meteor. Soc.*, **131**, 2961–3012, doi:10.1256/qj.04.176.
- Wang, B., and Q. Zhang, 2002: Pacific–East Asian teleconnection. Part II: How the Philippine Sea anomalous anticyclone is established during El Niño development. *J. Climate*, **15**, 3252–3265.
- , and T. Li, 2004: East Asian monsoon and ENSO interaction. *East Asian Monsoon*, C.-P. Chang, Ed., World Scientific, 172–212.
- , R. Wu, and X. Fu, 2000: Pacific–East Asia teleconnection: How does ENSO affect East Asian climate? *J. Climate*, **13**, 1517–1536.
- Watanabe, M., and T. Nitta, 1999: Decadal changes in the atmospheric circulation and associated surface climate variations in the Northern Hemisphere winter. *J. Climate*, **12**, 494–509.
- , and F.-F. Jin, 2003: A moist linear baroclinic model: Coupled dynamical–convective response to El Niño. *J. Climate*, **16**, 1121–1139.
- Wu, B.-Y., and J. Wang, 2002: Winter Arctic Oscillation, Siberian High and East Asian winter monsoon. *Geophys. Res. Lett.*, **29**, 1897, doi:10.1029/2002GL015373.
- , R. Zhang, and R. D’Arrigo, 2006: Distinct modes of the East Asian winter monsoon. *Mon. Wea. Rev.*, **134**, 2165–2179.
- Wu, R., J. L. Kinter III, and B. P. Kirtman, 2005: Discrepancy of interdecadal changes in the Asian region between the

- NCEP–NCAR reanalysis and observations. *J. Climate*, **18**, 3048–3067.
- Wu, Z., J. Li, B. Wang, and X. Liu, 2009: Can the Southern Hemisphere annular mode affect Chinese winter monsoon? *J. Geophys. Res.*, **114**, D11107, doi:10.1029/2008JD011501.
- Yang, S., K. M. Lau, and K. M. Kim, 2002: Variations of the East Asian jet stream and Asian–Pacific–American winter climate anomalies. *J. Climate*, **15**, 306–325.
- Yasunari, T., 1991: The monsoon year: A new concept of the climate year in the tropics. *Bull. Amer. Meteor. Soc.*, **72**, 1331–1338.
- Zhang, R., A. Sumi, and M. Kimoto, 1996: Impact of El Niño on the East Asian monsoon: A diagnostic study of the '86/87 and '91/92 events. *J. Meteor. Soc. Japan*, **74**, 49–62.
- Zhang, Y., K. Sperber, and J. Boyle, 1997: Climatology and interannual variation of the East Asian winter monsoon: Results from the 1979–95 NCEP/NCAR reanalysis. *Mon. Wea. Rev.*, **125**, 2605–2619.